Construction and Building Materials 527 (2026) 146380

Contents lists available at ScienceDirect

Construction and Building Materials

journal homepage: www.elsevier.com/locate/conbuildmat

Dynamic tensile behavior of ultra-high performance concrete reinforced with steel fibers under quasistatic to high strain rates

Ming-Hui Lee [a], Yuan-Jung Hsu [a,b], Huang Hsing Pan [c,*], Yi-Chun Lai [b], You-Shen Cheng [c]

[a] Department of Civil Engineering, National Pingtung University of Science and Technology, Pingtung 912301, Taiwan
[b] Department of Civil Engineering, R.O.C. Military Academy, Kaohsiung 830208, Taiwan
[c] Department of Civil Engineering, National Kaohsiung University of Science and Technology, Kaohsiung 807618, Taiwan

ARTICLE INFO

Keywords:
Ultra-high performance concrete
Strain rate sensitivity
Tension stress–strain curve
Steel fiber
Fracture energy

ABSTRACT

This study evaluated the tensile stress–strain behavior of ultra-high performance concrete (UHPC) specimens reinforced with steel fibers at strain rates ranging from 1.43×10^{-6} to $100\,s^{-1}$. UHPC specimens were prepared with steel fiber volume fractions of 0%, 1%, 2%, and 3%. Dog-bone-shaped specimens were fabricated to facilitate direct tensile testing and to characterize the tensile stress–crack responses, failure modes, dynamic increase factor (DIF) values, and fracture energies. The experimental results revealed that the UHPC specimens with steel fibers exhibited ductile behavior and a pronounced strain-softening region under dynamic tensile loading. In UHPC specimens incorporating steel fibers, both the initial and peak cracking strengths increased with strain rate, whereas the peak strain decreased. The addition of steel fibers increased peak strain at static and intermediate strain rates, although this effect was reduced at high strain rates ($>10\,s^{-1}$). At quasistatic and intermediate strain rates, both absorbed and fracture energies increased with fiber content and strain rate. At high strain rates, these energies decreased with increasing fiber content. A trilinear model was employed to represent the tensile strain-softening behavior of UHPC under dynamic loading. Except for the UHPC specimen containing $< 3\%$ steel fibers subjected to high strain rates, the model accurately estimated UHPC fracture energy under these conditions. A modified predictive equation was proposed to relate strain rate and steel fiber content to the DIF of UHPC.

1. Introduction

Ultra-high performance concrete (UHPC) exhibits markedly superior performance compared to conventional concrete [1–3]. A cement-based composite, UHPC exhibits high compressive strength, durability, and constructability, rendering it suitable for high-performance structural applications. The deformation and load-bearing behavior of UHPC throughout its service life can be characterized by using stress–strain curves. Information on key mechanical properties, such as elastic modulus, ultimate strength, initial crack strength (ICS), peak crack strength (PCS), deformation capacity, and ductility, can be obtained from such curves. For example, Ren et al. [4] employed six sizes of split Hopkinson pressure bar (SHPB) devices to conduct compression experiments and generate a UHPC compression strain curve. Using LS-DYNA software, they simulated the local stress–strain response to develop an analytical model of UHPC. However, their model did not simulate tensile behavior, a more complex physical phenomenon. To investigate UHPC tensile behavior, Chen et al. [5] conducted splitting tests to evaluate the effects of macro basalt fibers and hybrid fibers on UHPC mechanical properties at high temperatures. Additionally, Mezzal et al. [6] conducted flexural tests to evaluate the influence of recycled mixed steel fibers on the tensile and strain-hardening behavior of high-strength self-compacting concrete. Cadoni et al. [7] also conducted direct tensile tests to examine the tensile behavior of ultra-high-performance fiber-reinforced concrete under high strain rates. In the aforementioned studies and in the literature more broadly, splitting and bending tests have been commonly applied due to their simplicity; however, the resulting data inadequately capture the tensile behavior of UHPC. By contrast, direct tensile tests yield more comprehensive and precise data, although the required setup and implementation are substantially more complex.

The stress–strain behavior of UHPC depends on mix proportions, curing conditions, fiber content and type, and loading rates. Studies have demonstrated the critical role of steel fibers in the performance of

* Corresponding author.
E-mail address: pam@nkust.edu.tw (H.H. Pan).

https://doi.org/10.1016/j.conbuildmat.2026.146380
Received 2 January 2026; Received in revised form 18 March 2026; Accepted 14 April 2026

UHPC [8–11]. For example, Amanjean et al. [8] evaluated the influence of varying steel fiber contents and mixture designs on ultra-high-performance fiber-reinforced concrete. Additionally, Lu et al. [9] investigated the effect of various curing conditions on the properties of UHPC. Tayeh et al. [10] incorporated three types of steel fibers—straight, hooked, and corrugated—as experimental variables. Finally, Du et al. [11] explored how material proportions, curing methods, fiber dosage, and fiber morphology alter the shape of the stress–strain curve.

In UHPC without steel fibers, the stress–strain curve does not reveal pronounced strain-hardening behavior after cracking and exhibits a steep stress decline after peak strength is reached. Under tensile loading, steel fibers induce bridging that inhibits crack propagation; the resulting crack morphology is correlated with fiber content [12]. During the initial stages of crack initiation, microcracks and inherent microscopic defects within the concrete matrix tend to generate localized stress concentrations. Randomly distributed steel fibers within the matrix can effectively disperse stress concentrations and provide initial bridging resistance, thereby restraining the propagation and coalescence of microcracks. As a result, higher stress levels are required to drive further crack development. The presence of steel fibers delays the onset of visible cracking and enhances the material's resistance to cracking. Steel fibers thus markedly reduce initial cracking and enhance PCS. UHPC reinforced with steel fibers exhibits strain-hardening and softening phases in the stress–strain curve; this is because the fibers offset the abrupt stress reduction after cracking and extend the strain-softening region [13].

Strain-rate conditions also play a crucial role in influencing the mechanical performance of UHPC. In practical engineering applications, quasistatic strain rates primarily represent the slow loading conditions experienced by structures during normal service. Moderate strain rates correspond to the deformation rate range typically associated with structural members subjected to seismic loading. In contrast, high strain rates are commonly used to simulate extreme dynamic loading scenarios, such as blast events or high-velocity impacts. Therefore, systematically investigating the tensile behavior of UHPC over a wide range of strain rates enables a more comprehensive characterization of its mechanical response under conditions ranging from normal service environments to extreme loading scenarios. Such investigations contribute to improving the reliability and applicability of UHPC in seismic-resistant and protective structural design [14].

The mechanical properties of UHPC are sensitive to applied strain rate, which substantially influences the material's stress–strain response. Quasistatic tests facilitate the evaluation of failure modes and long-term mechanical characteristics. However, such tests fail to adequately capture dynamic behavior. A comprehensive characterization of UHPC across various strain rates is essential for accurately simulating its performance under dynamic conditions. Dynamic mechanical testing of UHPC primarily involves high-speed compression [14,15]. For example, Sun et al. [16] conducted dynamic compression experiments to assess the combined effects of steel fiber content and strain rate on UHPC compressive strength, reporting a positive correlation among compressive strength, fiber content, and strain rate. Investigations into the direct tensile properties of UHPC have addressed both the volumetric influence of steel fibers [17,18] and the effects of varying strain rates at constant fiber content [19–21]. Rezakhani et al. [22] conducted quasistatic direct tensile tests to investigate the failure mechanisms and stress–strain characteristics of UHPC. Fujikake et al. [23] investigated the mechanical performance of reactive powder concrete (RPC) at various strain rates, maintaining a constant steel fiber volume, and proposed a trilinear softening model. Although the compressive behavior of UHPC has been extensively documented, its tensile behavior under dynamic conditions involving variable steel fiber volume ratios and strain rates remains underexplored.

The dynamic increase factor (DIF) is a key parameter used to characterize UHPC behavior under dynamic loading. The DIF is defined as the ratio of material strength at dynamic strain rates to that at quasistatic strain rates; it can be used to quantify the mechanical enhancement induced by rapid loading and to inform structural design under seismic or blast conditions. For example, Wang et al. [24] reported that when UHPC beams were subjected to dynamic loads, their strain rates increased from 10^{-3} to 10^{3} s^{-1}, and the corresponding DIF values increased from 1.8 to 3.4, indicating a marked strength enhancement at higher strain rates. Su et al. [25] similarly demonstrated that the DIF values of UHPC compressive strength increase with strain rate. Clark [26] compared DIF values for UHPC cured at normal and high temperatures, reporting DIF ranges of 1.73–2.95 and 1.21–2.45, respectively. Muthuraja et al. [27] utilized the SHPB to assess the compressive stress–strain behavior of UHPC at various ages under both static and high-strain-rate conditions. Their findings indicated that, after controlling for impact velocities, DIF values decreased with increasing specimen age. Groenveld [28] utilized the SHPB to investigate how the orientation of steel fibers affects the DIF of UHPC under dynamic compression. An additional study revealed that the shear strength of UHPC is sensitive to variations in strain rate during shear tests [29].

Although the aforementioned studies have pioneered tests of UHPC tensile behavior, studies addressing UHPC strain-rate sensitivity under tensile loading are lacking. Under dynamic tension, UHPC exhibits a pronounced increase in strength, unlike the DIF characteristics of conventional concrete. For example, Bischoff and Perry [30] demonstrated that high-strength concrete exhibits only modest strength gains under dynamic strain rates. Moreover, fiber volume fraction and type substantially influence the strain-rate sensitivity of fiber-reinforced concrete [31–35]. Regarding UHPC, Plauk and Materialpruefung [36], Malvar and Ross [37], and Park et al. [38] reported that DIF values under tension typically follow a two-stage, linearly ascending pattern.

Absorbed energy and fracture energy are key indicators of a structure's resistance to blast and impact. Accordingly, these metrics have been employed to evaluate the strength of UHPC. For example, Wille and Naaman [39] demonstrated that incorporating a suitable volume of steel fibers enhanced UHPC ductility and fracture energy. Additionally, the fiber type and volume fraction substantially influence both the absorbed and fracture energies. Zielinski [40] reported that fracture energy increases with increasing strain rate from quasistatic to 10^{0} s^{-1}. However, Tran et al. [41] observed a reduction in fracture energy in steel-fiber-reinforced UHPC at high strain rates (from 5 to 92 s^{-1}). Nevertheless, studies on the strain-rate effects in UHPC containing steel fibers have yet to adequately characterize its tensile mechanical behavior across the strain rate spectrum. Accordingly, to address this gap, the present study evaluated the complete tensile behavior of UHPC reinforced with steel fibers under quasistatic to high-strain-rate loading conditions. DIF values obtained under tensile loading were compared against Fujikake's model [23] to identify the dynamic enhancement trend across steel fiber volume ratios and assess strain rate sensitivity. Direct tensile tests were conducted using an MTS 819 high-speed testing system. UHPC specimens were prepared with steel fiber volume fractions of 0%, 1%, 2%, and 3% and subjected to tensile strain rates ranging from 1.43×10^{-6} to 100 s^{-1}. Tensile stress–strain curves were used to capture ICS, PCS, and crack displacement under dynamic tension. The DIF values of tensile strength, absorbed energy, and fracture energy were quantified. Strain-hardening and strain-softening behaviors were analyzed and fitted using simulation curves, and an equation was proposed to predict the DIF of UHPC as a function of strain rate and steel fiber content.

Furthermore, this study proposes an improved DIF relationship model that simultaneously accounts for strain rates spanning from quasistatic to high-strain-rate regimes, together with the influence of steel fiber content. The proposed model is established based on the complete evolution of mechanical behavior rather than relying solely on empirical fitting of tensile strength. Consequently, it improves predictive accuracy and enhances engineering applicability under varying loading-rate conditions.

2. Experiments

2.1. Materials

The UHPC used in this study comprised American Society for Testing and Materials (ASTM) Type I Portland cement, ground granulated blast-furnace slag (GGBFS), silica fume, and quartz sand. Cement and slag powder each constituted 50% of the total binder content. The quartz sand and silica fume had particle sizes of 212–300 and 0.1–0.2 μm, respectively. These particle size ranges represent the main particle composition, rather than strictly uniform particle sizes, and there may be slight variations outside these ranges due to natural gradation. The water-to-binder ratio was 0.19. The UHPC also contained a superplasticizer, a high-efficiency water-reducing agent formulated from polycarboxylic acid. The steel fiber was straight, measuring 13 mm in length, 0.2 mm in diameter, with an aspect ratio of 65, and exhibiting a tensile strength of greater than 2800 MPa. To evaluate the influence of steel fiber volume on the tensile performance of UHPC, mixtures with steel fiber volume fractions of 0%, 1%, 2%, and 3% were prepared and designated as F0, F1, F2, and F3, respectively (Table 1).

2.2. Specimen preparation and curing

To fabricate UHPC, raw powder materials and quartz sand were introduced into a mixing container and agitated at low speed for 5 min to ensure uniform dispersion. Fine powders are typically prone to agglomeration due to humidity and static charge, and premixing them with quartz sand mitigates this effect. A solution containing water and superplasticizer was gradually added to the mixing container, after which the materials were thoroughly mixed. After 5–6 min, the blend transitioned from dry to wet and was mixed for an additional 8 min until it formed a homogeneous slurry. Steel fibers were subsequently incorporated and mixed for an additional 5 min to achieve a uniform distribution.

After the slurry was prepared, a flow test was conducted to evaluate its fluidity. The slurry was cast into cubic and dog-bone-shaped steel molds to produce specimens for compression and direct tension tests. During molding, the surfaces were covered with plastic wrap to minimize moisture loss and shrinkage. For each mixture, three compression specimens (50 mm × 50 mm × 50 mm) and three dog-bone-shaped tensile specimens were prepared. The specimens were left at room temperature for 24 h. After demolding, they were cured in water at 90 °C for 72 h and then stored under air-exposed conditions until 28 days of age. Subsequently, compression and tensile tests were conducted.

2.3. Experiments

A flow test was conducted in accordance with ASTM C1437–20 to determine the UHPC flow value. This was achieved by measuring the longitudinal and transverse diameters of the slurry spread 2 min after removing the tapered mold. The flow value was calculated as the average of the two perpendicular diameters. Moreover, a compression test was conducted in accordance with ASTM C109 specifications. Specifically, a compression testing machine was used to apply load to 50-mm cube specimens at a rate of 20 MPa/min to determine the maximum compressive strength. Compressive strength was evaluated at 3, 7, and 28 days of age and reported as the average of three tests, along with the standard deviations.

Tensile tests were conducted using an MTS 819 servo-hydraulic testing machine, which primarily supports quasistatic testing due to limitations in mechanical performance and oil-source compensation. Under high-pressure nitrogen and servo valve gain, the system supports mechanical testing at strain rates of $< 200\,s^{-1}$. The geometry and dimensions of the dog-bone-shaped tensile specimens are illustrated in Fig. 1. Direct tensile tests were conducted at seven strain rates to characterize the quasistatic and dynamic tensile behavior of the UHPC specimens. The specimens were subjected to strain rates $\dot{\varepsilon}$ of $1.43 \times 10^{-6}s^{-1}$ (S1), $1.43 \times 10^{-5}s^{-1}$ (S2), $1.43 \times 10^{-2}s^{-1}$ (S3), $1.43 \times 10^{-1}s^{-1}$ (S4), $10^{0}\ s^{-1}$ (S5), $10\ s^{-1}$ (S6), and $100\ s^{-1}$ (S7). These rates covered quasistatic (S1 and S2), intermediate (S3, S4, and S5), and high-speed (S6 and S7) loading conditions.

A Kistler 9351B piezoelectric force gauge (load cell) was used to measure tensile force (Fig. 1). Because instrument stiffness and clamping boundary conditions can induce elastic deformation errors during testing, two linear variable differential transformer displacement meters (LVDTs) were employed to record specimen deformation. Tensile stress–strain curves for the specimens were derived by averaging the data from three dog-bone-shaped specimens tested at each strain rate.

High-strain-rate direct tensile tests were conducted under displacement-controlled conditions. The LVDT displacement meter was

Table 1
Mix proportions of UHPC. (kg/m^3).

UHPC	Steel fiber (vol%)	Cement	GGBFS	Silicon fume	Sand	Water	SP	Steel fiber
F0	0	607	607	303	561	231	18	0
F1	1							78
F2	2							156
F3	3							234

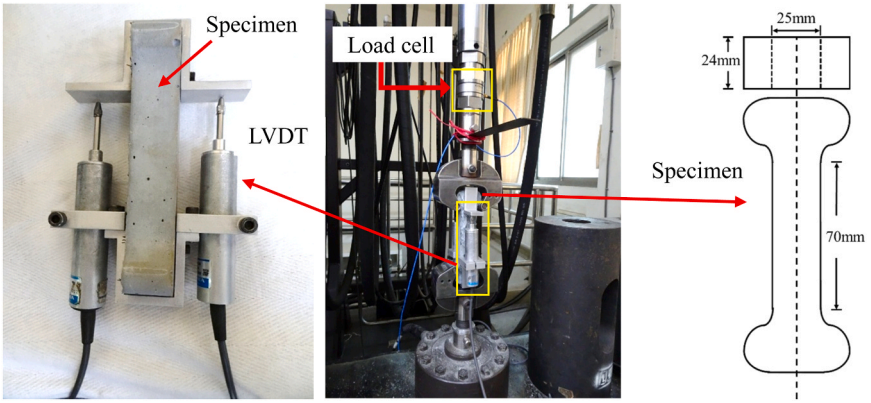

Fig. 1. Dynamic tensile test setup and dog-bone specimen.

installed within the specimen gauge length to directly measure specimen deformation. The data acquisition system operated at a high sampling frequency to accurately capture transient responses during dynamic loading. In addition, the load–time histories were carefully examined to verify the absence of significant oscillations or phase lag during testing. The axial alignment of the loading fixtures was also precisely calibrated to minimize potential vibrations and inertial disturbances induced by eccentric loading.

3. Results and discussion

3.1. Flow value

Fig. 2 presents the flow values of the UHPC specimens. The average flow value of the UHPC specimen without steel fibers (F0) was 275 mm, indicating high fluidity. Incorporation of 1% steel fiber (F1) reduced the flow value to 255 mm, reflecting a 7.3% decrease in fluidity. When the steel fiber volume fraction was 2% (F2) and 3% (F3), the flow values further decreased to 225 and 182 mm, respectively. These findings suggest that increasing the fiber content of UHPC enlarges the contact surface area between fibers and the slurry, thereby reducing the slurry's filling capacity. Additionally, friction and repulsion between steel fibers reduce slurry fluidity [22].

3.2. Compressive strength

Fig. 3 illustrates the influence of steel fiber content on the compressive strength of the UHPC specimens. At 28 days of age, the UHPC specimen without steel fibers exhibited a strength of 131.8 MPa. The inclusion of 1% steel fiber increased the strength to 160.1 MPa, and 3% steel fiber to 192.3 MPa. These findings suggest that a higher steel fiber content can promote a denser fiber distribution in the matrix, thereby inhibiting crack propagation. The study also observed that curing UHPC specimens in water heated to 90 °C accelerated the pozzolanic reaction, resulting in substantial compressive strength during the early curing period, up to day 3. Although strength gains persisted beyond this point, the rate of increase diminished because of reduced pozzolanic activity. Strength continued to increase from days 7–28 due to the equal proportions of GGBFS and cement in the binder, which facilitated a secondary pozzolanic reaction between GGBFS and calcium hydroxide.

3.3. Direct tensile stress–strain curve

The tensile stress–strain curves in Fig. 4 illustrate the dynamic behavior of the UHPC specimens at the seven evaluated strain rates. As indicated in Fig. 4(a), the UHPC specimen without steel fibers (F0) exhibited low ductility and underwent near-immediate fracture upon failure, with peak strain values of < 0.0004 (0.04%). The tensile stress–strain curves of F0 served as a control for comparison with those of the steel-fiber-reinforced UHPC specimens. For all fiber-reinforced UHPC specimens, peak tensile stress increased with the strain rate, and the corresponding peak strain decreased. The lowest peak strain occurred under high-speed loading at S7 ($\dot{\varepsilon} = 100\ s^{-1}$).

Fujikake et al. [23] investigated the tensile behavior of RPC (reactive powder concrete) with 2% steel fiber content at strain rates ranging from 1×10^{-6}(quasistatic) to $0.5\ s^{-1}$. Their results revealed a linear tensile stress–elongation curve up to the ICS, after which tensile stress increased slightly to the peak tensile strength. As displayed in Figs. 4(b)–4(d), the present study observed a similar behavior that persisted even at the high strain rate (S7). The stress–strain relationship remained linear up to the initial cracking point. The UHPC specimens with steel fibers exhibited strain-hardening behavior between the ICS and the PCS at all strain rates other than S7. Strain hardening between ICS and PCS occurs due to cracking, which gradually transfers stress from the concrete to the steel fibers. This transfer enhances the strength of UHPC because the steel fibers are stronger than the concrete. Strain hardening at S6 and S7 was nonsignificant because insufficient time was provided for the UHPC to develop microcracks or experience internal displacement during loading. Nevertheless, the strain-hardening range narrowed as the strain rate increased. Slight curve fluctuations after the initial cracking were attributable to the formation of fine internal cracks and progressive fiber pullout. As the load approached the peak failure strength, the load-bearing capacity of the steel fibers gradually weakened, thereby reducing the UHPC strength and inducing strain softening. The steel fibers continued to exert a bridging effect, compensating for the stress reduction caused by cracking, until the fibers failed.

The strain-softening behavior of UHPC is linked to its steel fibers and the strain rate. As presented in Fig. 5, the tensile strength of the UHPC specimens increased as the percentage of steel fibers increased. Cracking in concrete results from its inherently low tensile strength. Steel fibers enhance UHPC by providing additional tensile strength and facilitating crack bridging, thereby inhibiting crack propagation and improving tensile performance.

Although the strain-softening region in the tensile stress–strain curve was minimal in the UHPC specimen without steel fibers (F0), the incorporation of steel fibers markedly increased the strain-softening effect. As the fiber content increased, the strain corresponding to peak tensile stress became more pronounced. At the quasistatic strain rates

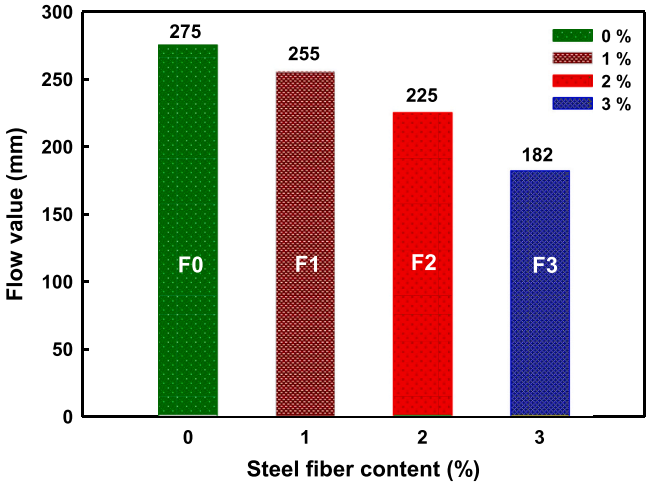

Fig. 2. The fluidity of UHPC.

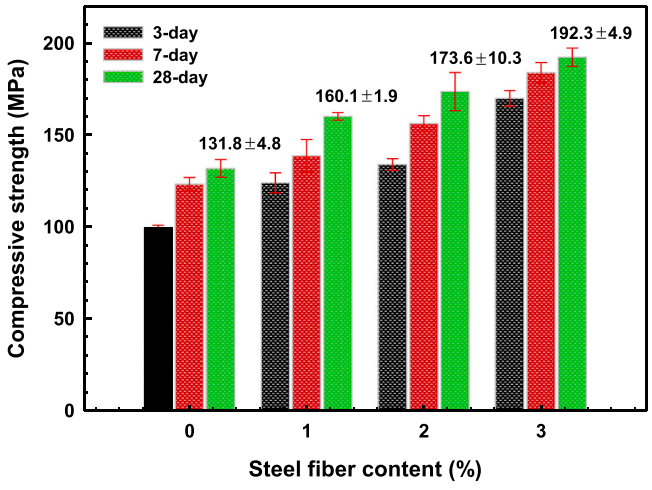

Fig. 3. Effect of steel fiber on compressive strength of UHPC.

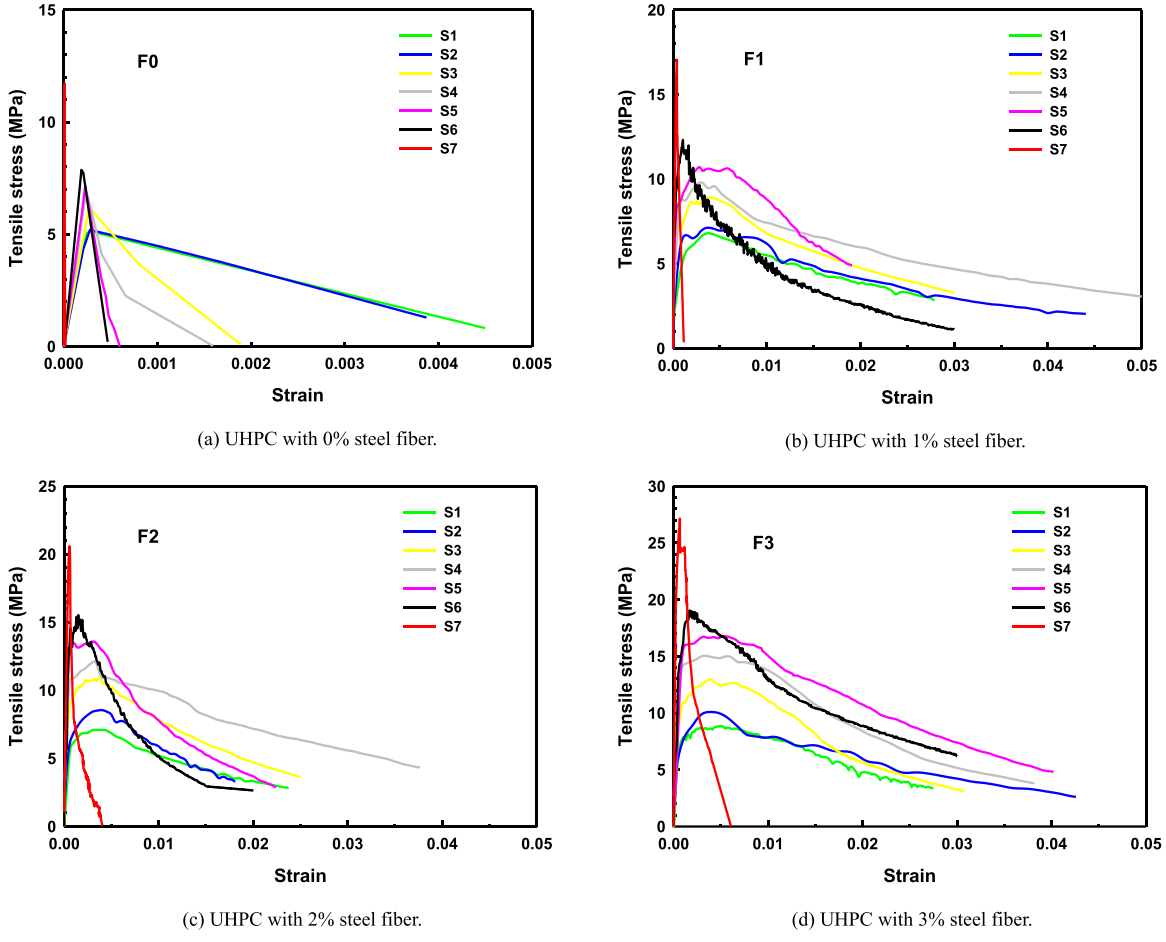

(a) UHPC with 0% steel fiber.

(b) UHPC with 1% steel fiber.

(c) UHPC with 2% steel fiber.

(d) UHPC with 3% steel fiber.

Fig. 4. Effect of strain rate on tensile stress-strain curves of UHPC.

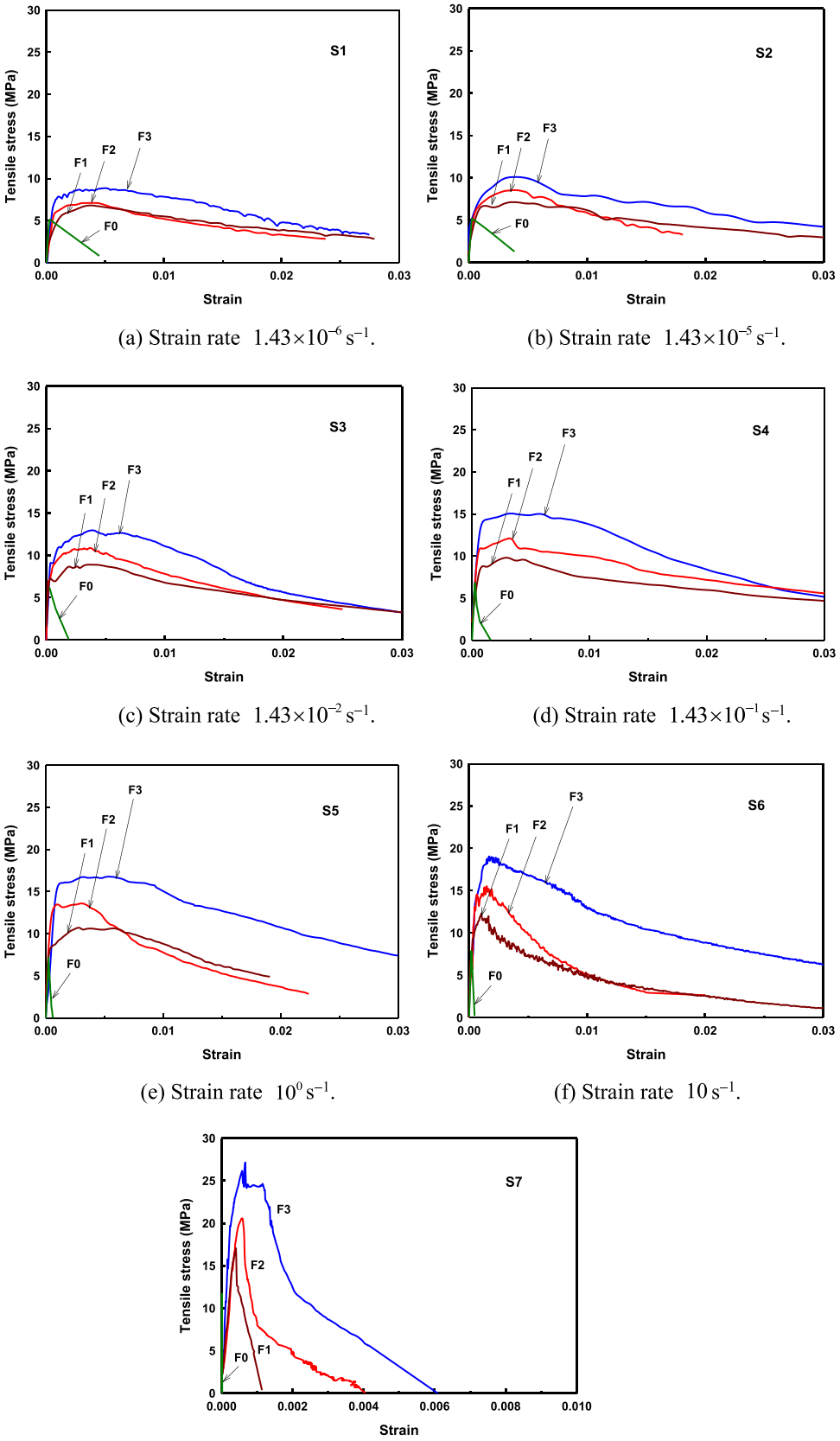

(a) Strain rate $1.43\times10^{-6}\,s^{-1}$.

(b) Strain rate $1.43\times10^{-5}\,s^{-1}$.

(c) Strain rate $1.43\times10^{-2}\,s^{-1}$.

(d) Strain rate $1.43\times10^{-1}\,s^{-1}$.

(e) Strain rate $10^{0}\,s^{-1}$.

(f) Strain rate $10\,s^{-1}$.

(g) Strain rate $100\,s^{-1}$.

Fig. 5. Effect of steel fibers on tensile stress-strain curves of UHPC.

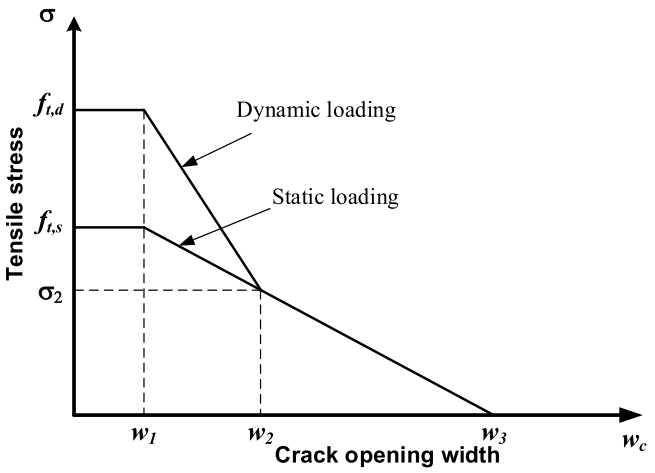

Fig. 6. The tensile stress-crack opening curve of the trilinear curve model.

(S1 and S2), the tensile stress–strain curves of the UHPC specimens with varying fiber content exhibited minimal differences; however, at the high strain rates (S6 and S7), disparities between the curves were evident. The most substantial divergence occurred at S7, indicating the high sensitivity of UHPC tensile strength to high strain rates.

3.4. Strain-softening behavior

Fujikake et al. [23] introduced a trilinear model to characterize the tensile strain-softening behavior of RPC with 2% steel fiber content (Fig. 6). The parameters w_1, w_2, w_3, and σ_2 were not arbitrarily fitted but were identified based on the experimentally obtained crack-opening behavior. The first softening-stage parameter, w_1, was determined from the tensile stress-crack opening curve at the inflection point where the stress begins to decrease rapidly. As the rate of stress reduction becomes less pronounced, the corresponding crack width is defined as w_2, at which the residual stress is denoted as σ_2. The complete softening point w_3 is defined as the crack width at which the tensile stress decreases to approximately zero. They substituted peak stress for strength before the point of ultimate failure. They set the quasistatic tensile strength $f_{t,s}$ to 10.8 MPa and evaluated the dynamic tensile strength $f_{t,d}$ by using w_1, w_2, and w_3 values of 0.4, 2.0, and 4.4 mm, respectively. In the early strain-softening stage, the tensile stress between w_1 and w_2 decreased rapidly. As the crack width increased to w_2, the tensile stress approached σ_2. Regardless of the strain rate, stresses $< \sigma_2$ in the second strain-softening stage were gradually reduced to zero.

The present study employed the aforementioned trilinear model to simulate strain-softening curves for the UHPC specimens at quasistatic (S1), intermediate (S4), and high-speed (S7) strain rates. Fig. 7 presents these curves. Although peak stress varied across different steel fiber content levels, the simulated curves (dashed lines) closely aligned with the experimental results (solid lines). This consistency verifies the

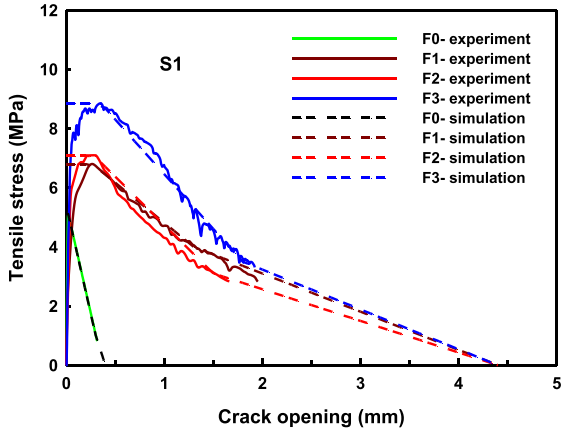

(a) At strain rate $1.43\times10^{-6}\,s^{-1}$.

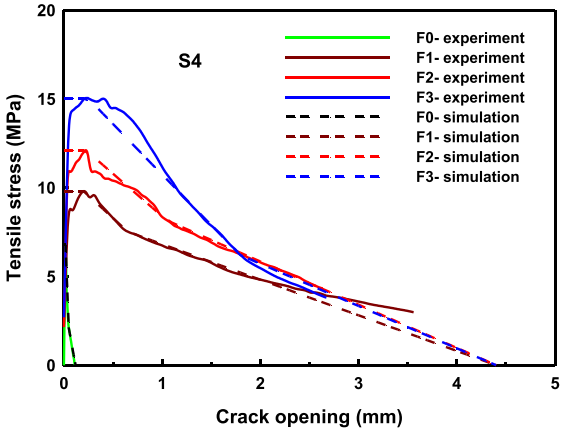

(b) At strain rate $1.43\times10^{-1}\,s^{-1}$.

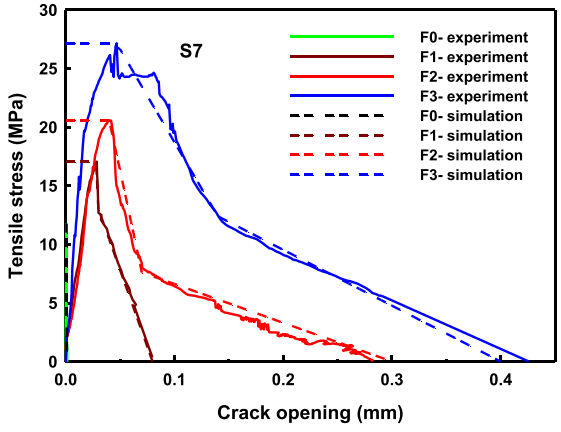

(c) At strain rate $100\,s^{-1}$.

Fig. 7. Comparison of experimental and trilinear simulation curves for strain-softening of UHPC under quasi-static, intermediate, and high strain rates.

Table 2
Simulation parameters of the trilinear strain-softening model.

Strain rate	UHPC	$f_{t,d}$	w_1	σ_2	w_2	w_3
S1	F0	5.11	0.021	1.02	0.30	0.40
	F1	6.80	0.260	4.00	1.30	4.40
	F2	7.71	0.280	3.10	1.50	4.40
	F3	8.86	0.350	3.50	1.80	4.40
S2	F0	5.19	0.019	2.86	0.17	0.40
	F1	7.13	0.250	4.27	1.30	4.40
	F2	8.55	0.270	3.28	1.30	4.40
	F3	10.11	0.287	5.21	1.60	4.40
S3	F0	6.21	0.018	2.46	0.08	0.15
	F1	8.91	0.250	5.88	1.00	4.40
	F2	10.87	0.259	5.51	1.20	4.40
	F3	12.97	0.270	5.66	1.40	4.40
S4	F0	6.78	0.017	2.11	0.05	0.12
	F1	9.81	0.200	7.52	0.65	4.40
	F2	12.11	0.220	8.15	1.05	4.40
	F3	15.05	0.240	6.19	1.80	4.40
S5	F0	7.17	0.016	1.35	0.033	0.045
	F1	10.71	0.196	6.29	1.000	3.000
	F2	13.58	0.217	4.55	1.200	3.000
	F3	16.73	0.220	9.87	1.500	4.000
S6	F0	7.87	0.013	3.65	0.024	0.035
	F1	12.31	0.073	4.24	0.820	2.500
	F2	15.52	0.105	3.76	0.910	2.700
	F3	19.05	0.119	10.95	0.960	3.500
S7	F0	11.70	0.0007	2.65	0.0009	0.0014
	F1	17.05	0.028	13.06	0.030	0.080
	F2	20.58	0.040	7.61	0.070	0.300
	F3	27.15	0.046	12.39	0.140	0.400

model's effectiveness in capturing the tensile strain-softening behavior of UHPC at various strain rates and fiber volumes. The simulation parameters for each trilinear curve are listed in Table 2. At a constant strain rate, the crack width w_1 increased with the volume of steel fibers. However, at higher strain rates, w1 decreased. The crack widths w_2 and w_3 exhibited similar trends. Additionally, the reduction in w_3 was more pronounced after the strain rate reached 1 s^{-1}, indicating that the strain-softening behavior of UHPC became less pronounced at high tensile strain rates.

The aforementioned trilinear model employed in this study is not merely a curve-fitting approach but rather a simplified constitutive formulation derived from the mechanisms of crack development and fiber pull-out in fiber-reinforced cementitious composites. The model has some predictive capability. The experimental results indicate that the model parameters exhibit consistent, physically meaningful variations with strain rate and steel fiber volume fraction, enabling the model to reasonably capture strain-softening behavior under different loading conditions. Nevertheless, although the aforementioned trilinear model framework captures the three-stage mechanisms of matrix cracking, fiber bridging, and fiber pull-out failure in fiber-reinforced composites, thereby demonstrating a degree of general applicability, the corresponding parameters remain closely tied to the type, geometry, and mechanical properties of the steel fibers. Consequently, parameter recalibration is still required when the model is applied to different fiber types or mixture design conditions.

3.5. Dynamic tensile properties

Fig. 8 displays a representative direct tensile stress–strain curve of UHPC containing steel fibers, demonstrating the material tensile strength, strain-hardening behavior, and strain-softening behavior [42,43]. The initial crack strength (ICS) is defined as the stress at which discernible cracks first appear in the UHPC matrix, representing the critical point at which the material transitions from the linear elastic to the multiple-crack development stage. The peak crack strength (PCS), in contrast, is defined as the maximum stress observed on the direct tensile stress–strain curve. This value reflects the maximum overall

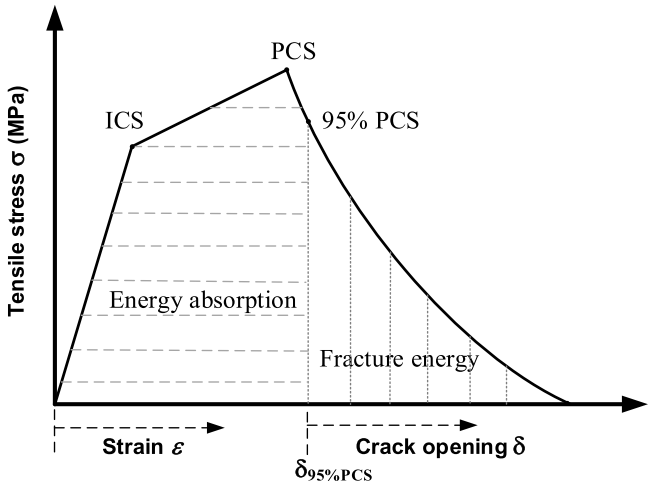

Fig. 8. Schematic diagram of a typical tensile stress-strain curve of UHPC.

load-carrying capacity resulting from the combined effects of steel-fiber bridging and the development of multiple cracks. When tensile loading exceeded the UHPC matrix's strength, cracking occurred. At the onset of cracking, internal stress was transferred to the steel fibers, inducing strain hardening. The stress within this range exceeded the ICS, promoting additional cracking that propagated from the UHPC matrix into the steel fibers. These fibers resisted crack growth and redistributed stress, altering the internal stress and displacement fields and modifying crack trajectories. During loading, the randomly distributed steel fibers acted as obstacles that inhibited crack development and sustained strain-hardening behavior. Upon reaching PCS, the fiber-bridging mechanism progressively weakened as multiple cracks localized. This localization accelerated crack propagation and initiated the strain-softening phase, leading to failure. The bridging action of the steel fibers enhanced ductility and load-bearing capacity during this process, increasing fracture energy [12].

Energy absorption (EA) was calculated as the area under the stress–strain curve encompassing the elastic deformation and strain-hardening phases preceding UHPC failure. When the stress in the specimen reaches the peak crack strength (PCS), microcracks have already initiated and are gradually accumulating; however, the dominant crack has not yet fully developed and therefore does not yet govern the overall failure behavior of the specimen. Pyo et al. [44] found that when the stress drops to about 95% of the peak strength, a dominant crack typically forms, and the specimen enters the continuous strain softening stage. To avoid the effects of crack localization and the unstable fluctuations typically observed during the early stage of post-peak softening, the EA is defined as the area under the stress-strain curve up to the point where the stress decreases to 95% of the PCS (Fig. 8). This value serves as the upper limit for the energy integration. The ICS, PCS, and peak strain (PS), and EA values at 95% PCS are listed in Table 3; the units for strength and EA are MPa and kJ/m^3, respectively. At each strain rate, the association between tensile strength (ICS and PCS) and steel fiber content was positive, and the specimen with a steel fiber volume fraction of 3% exhibited the highest tensile strength and the most significant increase in strength. For each UHPC specimen, tensile strength increased with increasing strain rate, with a strain rate of 100 s^{-1} yielding optimal results. The PCS and strain increased with increasing steel fiber content, as indicated in Table 3 and Fig. 7. The specimen with a steel fiber volume fraction of 3% exhibited the highest peak strain, indicating the best tensile properties. Although the PCS of each UHPC specimen was highest at high strain rates, the PS decreased with increasing strain rate. As shown in Table 3, UHPC specimens with higher steel fiber content exhibited higher EA values. At the quasistatic (S1 and S2) and intermediate (S3, S4, and S5) strain rates, EA increased with strain rate.

Table 3
Dynamic tensile properties of UHPC.

Strain rate	Properties	F0	SD	F1	SD	F2	SD	F3	SD
	ICS	5.06	0.32	5.44	0.31	6.10	0.28	7.59	0.29
	PCS	5.11	0.38	6.80	0.33	7.71	0.34	8.86	0.31
S1	PS	0.03%	0.0031	0.38%	0.026	0.40%	0.031	0.50%	0.028
	95%PCS	4.85	-	6.46	-	7.32	-	8.42	-
	EA	0.76	-	20.76	-	24.60	-	39.12	-
	ICS	5.11	0.37	6.12	0.24	7.05	0.35	9.13	0.35
	PCS	5.19	0.35	7.13	0.29	8.55	0.33	10.11	0.38
S2	PS	0.028%	0.0037	0.37%	0.035	0.39%	0.028	0.41%	0.033
	95%PCS	4.93	-	6.77	-	8.12	-	9.60	-
	EA	0.79	-	22.81	-	28.47	-	40.63	-
	ICS	5.44	0.35	7.24	0.29	8.64	0.31	10.91	0.33
	PCS	6.21	0.29	8.91	0.41	10.87	0.35	12.97	0.30
S3	PS	0.027%	0.0034	0.365%	0.042	0.37%	0.038	0.39%	0.035
	95%PCS	5.89	-	8.46	-	10.32	-	12.32	-
	EA	0.84	-	28.92	-	35.93	-	43.13	-
	ICS	6.34	0.27	8.25	0.33	10.91	0.44	13.81	0.55
	PCS	6.78	0.29	9.81	0.39	12.11	0.48	15.05	0.60
S4	PS	0.025%	0.0038	0.292%	0.039	0.32%	0.041	0.35%	0.044
	95%PCS	6.44	-	9.32	-	11.50	-	14.30	-
	EA	0.88	-	32.53	-	36.13	-	46.70	-
	ICS	6.68	0.37	9.17	0.38	12.46	0.50	15.53	0.62
	PCS	7.17	0.41	10.71	0.43	13.58	0.55	16.73	0.67
S5	PS	0.023%	0.0041	0.28%	0.035	0.31%	0.033	0.315%	0.041
	95%PCS	6.81	-	10.17	-	12.90	-	15.89	-
	EA	0.86	-	35.19	-	38.72	-	48.59	-
	ICS	7.63	0.63	11.47	0.57	14.51	0.79	18.51	0.98
	PCS	7.87	0.68	12.31	0.53	15.52	0.85	19.05	1.05
S6	PS	0.019%	0.0052	0.105%	0.048	0.151%	0.052	0.17%	0.056
	95%PCS	7.48	-	11.69	-	14.74	-	18.09	-
	EA	0.72	-	10.10	-	18.05	-	23.56	-
	ICS	10.72	1.05	16.15	0.75	19.23	0.88	26.15	1.01
	PCS	11.70	1.10	17.05	0.82	20.58	0.81	27.15	1.14
S7	PS	0.0011%	0.00065	0.0407%	0.0051	0.0575%	0.0062	0.0669%	0.0058
	95%PCS	11.12	-	16.19	-	19.55	-	25.79	-
	EA	0.068	-	4.13	-	8.11	-	12.65	-

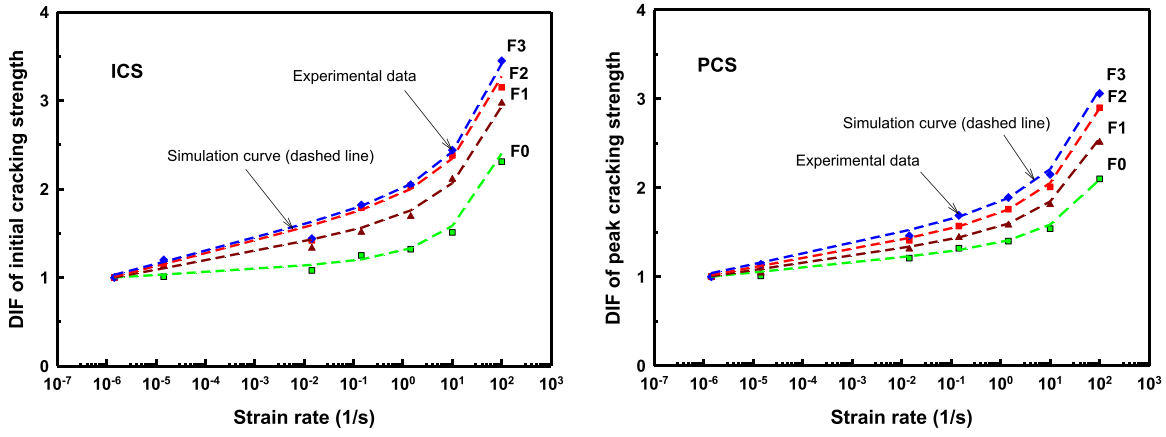

(a) DIF-strain rate curves of ICS. (b) DIF-strain rate curves of PCS.

Fig. 9. Comparison of experimental and simulated DIF-strain rate curves for ICS and PCS.

However, at the high strain rates (S6 and S7), the EA values decreased. This reduction in EA resulted from rapid crack propagation, which inhibited the steel fibers' bridging effect and compromised the material's EA capacity.

Furthermore, as observed in Table 3, under identical strain-rate conditions, the standard deviation (SD) of tensile strength increases slightly with increasing steel fiber volume fraction. This phenomenon can be attributed to a transition in the failure mechanism from matrix-dominated crack propagation to multiple cracking governed by steel-fiber bridging, in which the tensile response becomes more sensitive to fiber distribution, orientation, and pull-out behavior. Conversely, when the steel fiber volume fraction is fixed, the standard deviation tends to increase with increasing strain rate. At elevated strain rates, crack propagation becomes more localized, and the fiber pull-out process is significantly shortened. As a result, the effectiveness of the bridging mechanism becomes more dependent on the local distribution of steel fibers, thereby increasing the variability among specimens.

3.6. *Dynamic increase factor*

Concrete is susceptible to applied strain, and the DIF quantifies this sensitivity. A DIF value of greater than 1.0 indicates that strength

Table 4
DIF values for initial cracking strength and peak cracking strength.

Strain rate	Reference strength	F0	F1	F2	F3
S1	ICS	1.00	1.00	1.00	1.00
	PCS	1.00	1.00	1.00	1.00
S2	ICS	1.01	1.13	1.16	1.20
	PCS	1.01	1.04	1.11	1.14
S3	ICS	1.08	1.33	1.42	1.44
	PCS	1.21	1.31	1.41	1.46
S4	ICS	1.25	1.61	1.79	1.82
	PCS	1.32	1.44	1.57	1.69
S5	ICS	1.32	1.69	2.04	2.05
	PCS	1.40	1.58	1.76	1.89
S6	ICS	1.51	2.11	2.38	2.44
	PCS	1.54	1.81	2.01	2.15
S7	ICS	2.31	2.97	3.15	3.45
	PCS	2.10	2.51	2.90	3.06

increases with increasing strain rate. The strain rate sensitivity of concrete primarily derives from its intrinsic properties. Conventional high-strength concrete typically exhibits limited strength increase under dynamic loading conditions [30]. By contrast, in fiber-reinforced concrete, strain rate sensitivity is correlated with both fiber type and volume fraction [31–35]. As the applied strain rate in fiber-reinforced concrete increases, the material's resistance to deformation also increases.

Unlike conventional concrete, UHPC exhibits high DIF values (ICS and PCS) under tensile loading. Several regression equations have been derived based on the International Federation for Structural Concrete (FIB) model [36], the Malvar and Ross model [37], and the model of Park et al. [38] to estimate concrete DIF under dynamic and impact conditions. These models [36–38] have adopted a piecewise power-law function in their regression equations to ensure continuity at the inflection point of the DIF curve; this function is expressed as follows:

$$DIF = \begin{cases} (\dot{\varepsilon}/\dot{\varepsilon}_s)^a, & \dot{\varepsilon} \le d \\ b(\dot{\varepsilon}/\dot{\varepsilon}_s)^c, & \dot{\varepsilon} > d \end{cases} \quad (1)$$

where $\dot{\varepsilon}$ and $\dot{\varepsilon}_s$ represent the dynamic and static strain rates, respectively. The constants a, b, and c denote material-specific parameters, and d denotes the strain rate ranging between 1 and 30 s^{-1}. Experiments have demonstrated the presence of an inflection point at d in the UHPC DIF curve within the strain rate range of 1 and 100 s^{-1} [45]. Thomas and Sorensen [45] investigated the effect of strain rate on the tensile behavior of UHPC, specifically the DIF. They concluded that current models fit empirical data well at quasistatic and intermediate strain rates but tend to overestimate the DIF at high strain rates. This behavior is likely due to the increased strain rates generated during impact tests, which differ from those used in quasistatic and intermediate testing protocols. Additionally, Fujikake et al. [23] introduced a continuous power-law function to simulate the DIF, which can be expressed as follows:

$$\mathrm{DIF} = \left(\frac{\dot{\varepsilon}}{\dot{\varepsilon}_s}\right)^{p\left[\log\left(\frac{\dot{\varepsilon}}{\dot{\varepsilon}_s}\right)\right]^q} \quad (2)$$

where p and q are material parameters. Eqs. (1) and (2) apply only to the strain rate and do not calculate steel fiber content.

Fig. 9 illustrates simulated DIF curves (dashed lines) for the ICS and PCS of UHPC as functions of strain rate and steel fiber content. Both values increased with strain rate, with a more pronounced increase observed at high strain rates. For example, as the strain rate increased from 1.43×10^{-5} to 100 s^{-1}, the PCS DIF for F1 rose from 1.04 to 2.51, as indicated in Fig. 9(b). In the F0 specimen without steel fibers, both the ICS and PCS values increased substantially at high strain rates, particularly at rates beyond S5 (10^0 s^{-1}). In the fiber-reinforced UHPC specimens, substantial increases in DIF values occurred at the intermediate strain rates (S3–S5; Table 4).

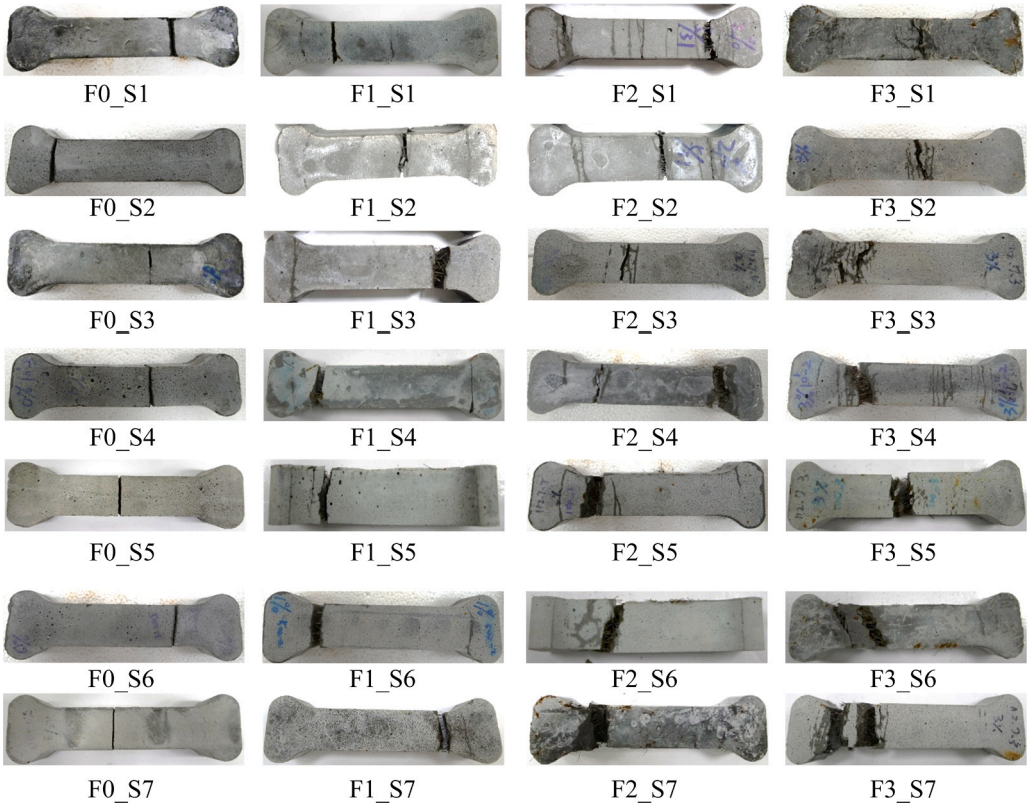

Fig. 10. Crack appearance of the UHPC specimen.

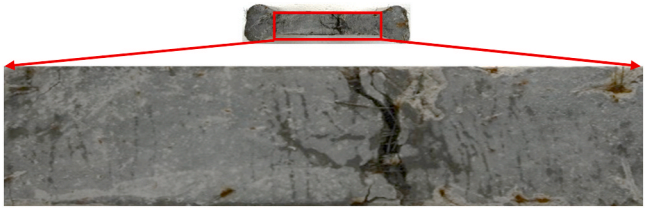

Fig. 11. Magnified image of specimen F3_S1.

Both strain rate and steel fiber content were noted to contribute to increased DIF values. At a tensile strain rate of 10 s^{-1} (S6), the PCS DIF value of F0 was 1.54. The corresponding PCS values for the UHPC specimens with steel fiber volume fractions of 1%, 2%, and 3% were 1.81, 2.01, and 2.15, respectively, representing increases of 17.5%, 30.5%, and 39.6% relative to the control (F0). As the strain rate increased, the DIF value of ICS in steel fiber-reinforced UHPC almost consistently exceeded that of PCS. The DIF–strain rate curves for both cracking strengths exhibited an upward trend after 10^0 s^{-1}.

DIF models such as those specified in Eqs. (1) and (2) incorporate strain rate effects alone and do not account for the presence of steel fiber. To address this limitation, a power law was used to account for the effects of strain rate and steel fiber content on DIF. The following simulation equation was developed to predict the DIF of UHPC incorporating steel fibers at volume fractions of 0%–3% and strain rates of 1.43×10^{-6} to 10^2 s^{-1}:

$$\mathrm{DIF} = f_1(c_1)\sqrt{\dot{\varepsilon}} + f_2(c_1)\log \dot{\varepsilon} + f_3(c_1) \tag{3}$$

where c_1 is the steel fiber volume fraction (%) in UHPC and f_1,f_2, andf_3 are quadratic polynomials in terms of c_1. Moreover, $\dot{\varepsilon}$ represents the applied strain rate. Fig. 9 illustrates the simulated DIF–strain rate curves (dashed lines) for ICS and PCS in the UHPC specimens with steel fibers. The material constants in Eqs. (4)–(9) were obtained using a trial-and-error method. For example, the ICS simulation curves in Fig. 9(a) were generated by substituting the steel fiber volume fraction c_1 into the following functions:

$$f_1(c_1) = 0.003c_1^2 - 0.006c_1 + 0.115 \tag{4}$$

$$f_2(c_1) = -0.017c_1^2 + 0.089c_1 + 0.032 \tag{5}$$

$$f_3(c_1) = 0.094c_1^2 + 0.514c_1 + 1.188 \tag{6}$$

where $\dot{\varepsilon} \geq 1 \times 10^{-6} s^{-1}$ in Eq. (3). The simulation curves for PCS in Fig. 9 (b) were calculated using the following functions involving the steel fiber volume fraction calculated in Eq. (3).

$$f_1(c_1) = -0.005c_1^2 + 0.031c_1 + 0.066 \tag{7}$$

$$f_2(c_1) = -0.002c_1^2 + 0.027c_1 + 0.055 \tag{8}$$

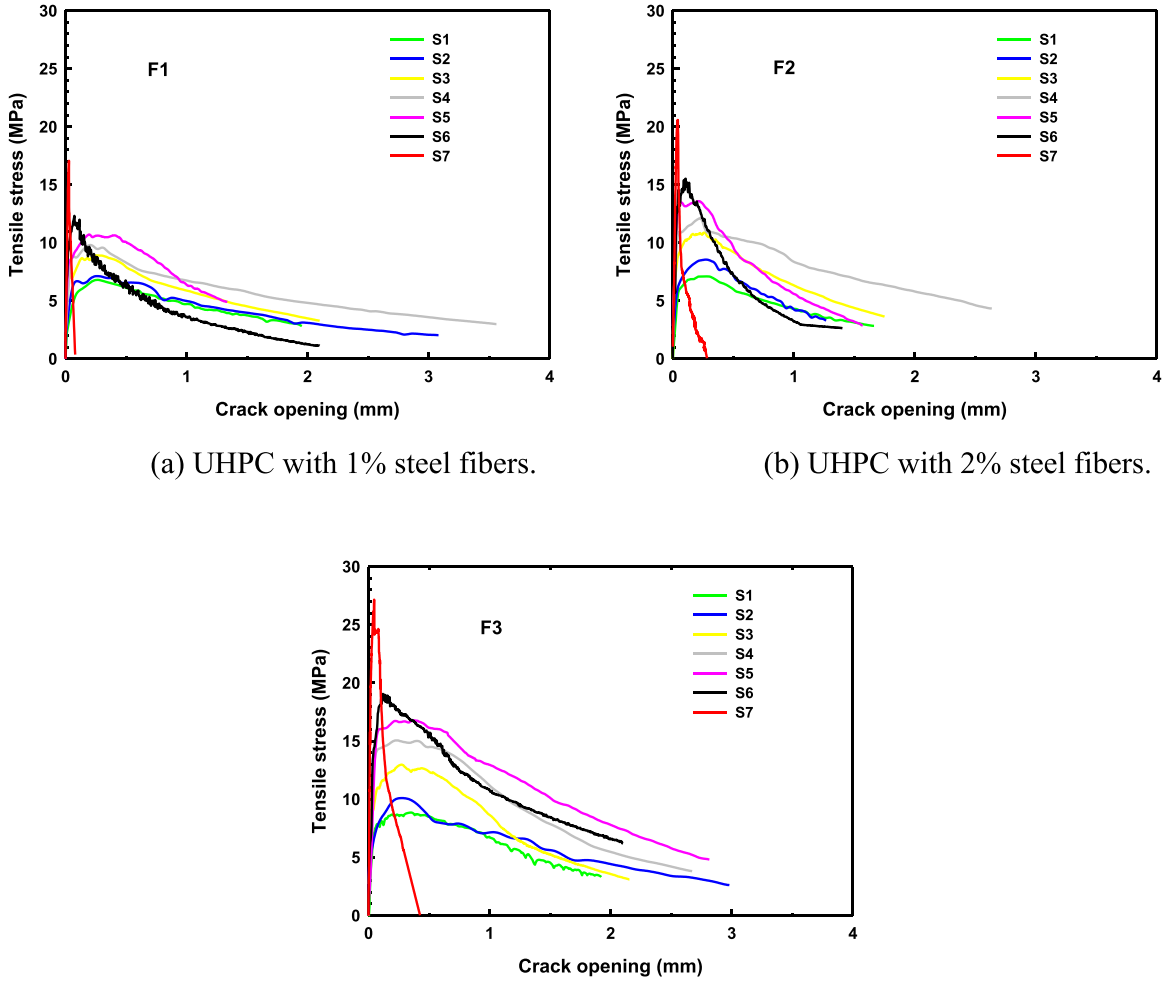

(a) UHPC with 1% steel fibers.

(b) UHPC with 2% steel fibers.

(c) UHPC with 3% steel fibers.

Fig. 12. Effect of strain rate on tensile stress-cracking opening curve.

Table 5
Fracture energy of UHPC. (Unit: kJ/m^3).

	F1_S1	Deviation	F2_S1	Deviation	F3_S1	Deviation
Experiment	6.66	1.8%	6.62	3.5%	9.35	3.9%
Simulation	6.78		6.85		8.99	
	F1_S2	Deviation	F2_S2	Deviation	F3_S2	Deviation
Experiment	7.28	1.2%	7.31	5.7%	9.43	2.8%
Simulation	7.37		7.73		9.69	
	F1_S3	Deviation	F2_S3	Deviation	F3_S3	Deviation
Experiment	8.97	2.7%	10.21	4.5%	12.83	2.3%
Simulation	9.21		10.67		12.53	
	F1_S4	Deviation	F2_S4	Deviation	F3_S4	Deviation
Experiment	9.80	0.6%	12.20	3.4%	16.12	3.7%
Simulation	9.86		12.62		15.53	
	F1_S5	Deviation	F2_S5	Deviation	F3_S5	Deviation
Experiment	10.65	7.3%	10.82	7.8%	18.05	3.2%
Simulation	9.87		11.66		17.48	
	F1_S6	Deviation	F2_S6	Deviation	F3_S6	Deviation
Experiment	7.07	14.7%	8.56	14.8%	15.93	0.8%
Simulation	8.11		9.83		16.06	
	F1_S7	Deviation	F2_S7	Deviation	F3_S7	Deviation
Experiment	0.64	29.6%	1.65	28.5%	4.44	6.3%
Simulation	0.83		2.12		4.72	

$$f_3(c_1) = -0.008c_1^2 + 0.160c_1 + 1.322 \quad (9)$$

These equations reveal that Eq. (3) is consistent with the experimental DIF curve values.

The coefficients of determination (R^2) of the DIF curves for both ICS and PCS in Fig. 9 exceed 0.9, indicating their validity. The proposed DIF model in Eq. (3) is most sensitive to dynamic strain rate. Nonlinear behavior of the DIF can be observed during dynamic loading. Fiber content affects material strength, with the most significant effect occurring in the 0–2 vol% range, while the strength-enhancing effect gradually weakens beyond 2 vol%. When the volume content of steel fibers exceeds 3%, fibers tend to agglomerate, increasing porosity in UHPC. The material's properties exhibit significant variability. To ensure the rationality and accuracy of the description of UHPC's dynamic load-bearing capacity, it is not recommended to extrapolate the proposed equations beyond 3% fiber content.

3.7. Crack patterns

Fig. 10 illustrates the fracture morphology of UHPC specimens subjected to direct tensile tests at the strain rates of S1–S7. The specimen without steel fibers (F0) exhibited a single, distinct fracture surface. By contrast, the UHPC specimens with steel fiber volume fractions of 1%, 2%, and 3% developed multiple cracks under tensile loading. When the strain rate was held constant, the number of cracks increased markedly with increasing steel fiber content. The specimen with a steel fiber volume fraction of 3% (F3) exhibited multiple fine microcracks. Under quasistatic conditions, the cracks were minor and more densely distributed (Fig. 11).

When the steel fiber volume remained constant, the crack formation in the UHPC specimens intensified at both quasistatic and intermediate strain rates. Nevertheless, at high strain rates (S6 and S7), the number of fine cracks decreased, and large cracks were visible. This reduction in microcracks may be due to the rapid application of tensile force, which caused failure before the steel fibers' bridging mechanism could compensate, thereby reducing microcrack development.

3.8. Fracture energy

Fiber-reinforced UHPC incorporates short steel fibers measuring 13 mm in length that inhibit crack propagation. Because the number of cracks was not quantified during testing, the direct tensile fracture energy was used as a proxy for resistance to cracking. Fracture energy was calculated as the total energy absorbed during the strain-hardening and strain-softening phases. At the strain rates of S1–S6, the fracture energy was determined over a crack opening length corresponding to the displacement from the ICS up to 1.3 mm. By contrast, at S7, the fracture energy was calculated over the entire strain-softening phase. Due to the significantly increased strain rate, crack propagation becomes more strongly localized. The pull-out time of the steel fibers is consequently shortened, leading to a rapid loss of the fiber-bridging effect and a rapid decrease in tensile stress to near zero. As a result, even when the integration includes the entire softening process, the additional energy contribution in the later stage remains very limited. Consequently, the overall fracture energy obtained for S7 is comparatively low.

As the strain rate increased, the area under the tensile stress–strain curve gradually expanded (Fig. 12). However, at high strain rates (e.g., S6 and S7), the area under the curve decreased substantially. As presented in Table 5, this reduction was most pronounced for specimen F1_S7 (F1 at strain rate S7) when the strain rate equaled or exceeded 10 s^{-1} (S6). Although the UHPC specimens exhibited higher peak tensile strength at higher strain rates, the corresponding peak strain declined because the accelerated crack propagation prevented the fiber-bridging mechanism from fully developing. Additionally, the fracture energy increased with steel fiber content and reached its maximum at 3% (Table 5), verifying that the addition of steel fibers substantially enhanced fracture energy.

The fracture energy corresponding to S1–S7 was estimated by using the trilinear softening model. Specifically, the area under the dashed curves in Fig. 7 and the simulated values listed in Table 5 were used to calculate the fracture energy. Comparisons between the experimental and simulated results revealed minimal deviations (<6%), except for F1 and F2 at strain rates above S5. Additionally, when the steel fiber volume fraction was increased to 3%, the trilinear model remained accurate even at high strain rates. These results indicate that the trilinear softening model provides a reliable method for estimating the fracture energy of UHPC (including contributions from both strain-hardening and strain-softening regions) across various steel fiber volumes and dynamic loading conditions.

4. Conclusions

Direct tensile tests were conducted to investigate the tensile behavior of UHPC reinforced with steel fibers at quasistatic and dynamic strain rates. Based on these tests, this study drew the following conclusions. (1) All UHPC specimens exhibited increased PCS at higher strain rates. Nevertheless, the corresponding strain decreased as the strain rate increased. The strain-hardening region expanded with increasing strain

rates in the fiber-reinforced UHPC but contracted at high strain rates (e.g., $>10\ s^{-1}$). (2) The inclusion of steel fibers enhanced the maximum tensile stress and extended the strain-softening region under dynamic loading. (3) When the strain rate was constant, crack opening width increased with steel fiber content. When the fiber content was constant, crack opening width decreased with increasing strain rate. (4) The experimental results confirm that the trilinear model accurately simulated the tensile strain-softening curve of UHPC at dynamic strain rates. (5) EA increased with strain rate in the quasistatic (S1 and S2) and intermediate (S3, S4, and S5) ranges. At high strain rates, UHPC exhibited reduced EA. (6) A modified equation was developed to estimate the association between DIF and strain rates; this equation incorporated steel fiber content and applied tensile strain rate. (7) The trilinear softening model reliably estimates UHPC fracture energy during both the strain-hardening and strain-softening phases under conditions of varied fiber content and dynamic loading. (8) At quasistatic and intermediate strain rates, the number of fracture cracks in UHPC increased markedly. At increased strain rates, the number of microcracks decreased, and wide cracks became visible. At each strain rate, greater steel fiber content was associated with a greater number of cracks. (9) Both the EA and fracture energy increased with steel fiber content and strain rate under quasistatic and intermediate conditions. At high strain rates (e.g., 10 and $100\ s^{-1}$), the rapid loading overwhelmed the steel fibers' bridging mechanism, reducing EA and fracture energy.

CRediT authorship contribution statement

Ming-Hui Lee: Validation, Resources, Methodology, Formal analysis. **Yuan-Jung Hsu:** Validation, Investigation, Data curation. **Huang Hsing Pan:** Writing – original draft, Validation, Supervision, Methodology, Conceptualization. **Yi-Chun Lai:** Validation, Investigation. **You-Shen Cheng:** Formal analysis, Data curation.

Declaration of Competing Interest

The authors declare that they have no known competing financial interests or personal relationships that could have appeared to influence the work reported in this paper.

Acknowledgements

This work was supported by the National Science and Technology Council of Taiwan under grant No. NSTC 113–2221-E-992–031.

Data availability

Data will be made available on request.

References

[1] D.Y. Yoo, N. Banthia, Mechanical properties of ultra-high-performance fiber-reinforced concrete: a review, Cem. Concr. Compos 73 (2016) 267–280.
[2] F.U.A. Shaikh, S. Luhar, H.Ş. Arel, I. Luhar, Performance evaluation of Ultrahigh performance fibre reinforced concrete–A review, Constr. Build. Mater. 232 (2020) 117152.
[3] D. Wang, C. Shi, Z. Wu, J. Xiao, Z. Huang, Z. Fang, A review on ultra high performance concrete: Part II. Hydration, microstructure and properties, Constr. Build. Mater. 96 (2015) 368–377.
[4] L. Ren, X. Yu, Z. Guo, L. Xiao, Numerical investigation of the dynamic increase factor of ultra-high performance concrete based on SHPB technology, Constr. Build. Mater. 325 (2022) 126756.
[5] Z. Chen, X. Wang, L. Ding, K. Jiang, X. Liu, J. Liu, Z. Wu, Spalling resistance and mechanical properties of ultra-high performance concrete reinforced with multi-scale basalt fibers and hybrid fibers under elevated temperature, J. Build. Eng. 77 (2023) 107435.
[6] S.K. Mezzal, Z. Al-Azzawi, K.B. Najim, Effect of discarded steel fibers on impact resistance, flexural toughness and fracture energy of high-strength self-compacting concrete exposed to elevated temperatures, Fire Saf. J. 121 (2021) 103271.
[7] E. Cadoni, D. Forni, E. Bonnet, S. Dobrusky, Experimental study on direct tensile behaviour of UHPFRC under high strain-rates, Constr. Build. Mater. 218 (2019) 667–680.
[8] E.N. Amanjean, M. Mouret, T. Vidal, Effect of design parameters on the properties of ultra-high performance fibre-reinforced concrete in the fresh state, Constr. Build. Mater. 224 (2019) 1007–1017.
[9] D. Lu, J. Zhong, B. Yan, J. Gong, Z. He, G. Zhang, C. Song, Effects of curing conditions on the mechanical and microstructural properties of ultra-high-performance concrete (UHPC) incorporating iron tailing powder, Materials 14 (1) (2021) 215.
[10] B.A. Tayeh, M.H. Akeed, S. Qaidi, B.A. Bakar, Ultra-high-performance concrete: Impacts of steel fibre shape and content on flowability, compressive strength and modulus of rupture, Case Stud. Constr. Mater. 17 (2022) e01615.
[11] W. Du, F. Yu, L. Qiu, Y. Guo, J. Wang, B. Han, Effect of steel fibers on tensile properties of ultra-high-performance concrete: a review, Materials 17 (5) (2024) 1108.
[12] J. Zhang, J. Chen, Dynamic tensile strength and failure mode of concrete at high strain rates: a review, J. Wuhan. Unv. Technol. Mater. 30 (5) (2015) 977–987.
[13] N.T. Tran, T.K. Tran, D.J. Kim, High rate response of ultra-high-performance fiber-reinforced concretes under direct tension, Cem. Concr. Res. 69 (2015) 72–87.
[14] Q. Yu, W. Zhuang, C. Shi, Research progress on the dynamic compressive properties of ultra-high performance concrete under high strain rates, Cem. Concr. Compos 124 (2021) 104258.
[15] J. Xiao, Z. Li, Q. Xie, L. Shen, Effect of strain rate on compressive behaviour of high-strength concrete after exposure to elevated temperatures, Fire Saf. J. 83 (2016) 25–37.
[16] K. Sun, Y. Wu, S. Li, Y. Feng, L. Feng, Study on dynamic impact mechanical properties of UHPC with high-content and directional reinforced steel fiber, Appl. Sci. 13 (6) (2023) 3753.
[17] G.M. Ren, H. Wu, Q. Fang, J.Z. Liu, Effects of steel fiber content and type on static mechanical properties of UHPCC, Constr. Build. Mater. 163 (2018) 826–839.
[18] G.D. Ashkezari, F. Fotouhi, M. Razmara, Experimental relationships between steel fiber volume fraction and mechanical properties of ultra-high performance fiber-reinforced concrete, J. Build. Eng. 32 (2020) 101613.
[19] Q. Li, X. Jiang, T. Zeng, S. Xu, Experimental investigation on strain rate effect of high-performance fiber reinforced cementitious composites subject to dynamic direct tensile loading, Cem. Concr. Res. 157 (2022) 106825.
[20] T.K. Tran, D.J. Kim, High strain rate effects on direct tensile behavior of high performance fiber reinforced cementitious composites, Cem. Concr. Compos 45 (2014) 186–200.
[21] S. Gurusideswar, A. Shukla, K.N. Jonnalagadda, P. Nanthagopalan, Tensile strength and failure of ultra-high performance concrete (UHPC) composition over a wide range of strain rates, Constr. Build. Mater. 258 (2020) 119642.
[22] R. Rezakhani, D.A. Scott, F. Bousikhane, M. Pathirage, R.D. Moser, B.H. Green, G. Cusatis, Influence of steel fiber size, shape, and strength on the quasi-static properties of ultra-high performance concrete: experimental investigation and numerical modeling, Constr. Build. Mater. 296 (2021) 123532.
[23] K. Fujikake, T. Senga, N. Ueda, T. Ohno, M. Katagiri, Effects of strain rate on tensile behavior of reactive powder concrete, J. Adv. Concr. Technol. 4 (1) (2006) 79–84.
[24] S. Wang, L. Shi, Y. Huang, S. Chen, Y. Tang, Dynamic behavior and dynamic enhancement factor of ultra-high-performance concrete beams under impact loads, Constr. Build. Mater. 261 (2020) 120155.
[25] Y. Su, J. Li, C. Wu, P. Wu, Z.X. Li, Influences of nano-particles on dynamic strength of ultra-high performance concrete, Compos. Part B 91 (2016) 595–609.
[26] J. Clark, Preliminary investigation of ultra-high performance concrete behavior at high strain rates using the split-Hopkinson pressure bar, Master's Thesis, Mich. Technol. Univ. (2013).
[27] M. Muthuraja, S. Ranjithkumar, S.N. Khaderi, S. Suriya Prakash, High-strain-rate compression behavior of ultrahigh-performance concrete at different ages, J. Mater. Civ. Eng. 36 (11) (2024) 04024349.
[28] A.B. Groeneveld, Effect of fiber orientation on dynamic compressive properties of an ultra-high performance concrete, Master's Thesis, Mich. Technol. Univ. (2016).
[29] S.G. Millard, T.C.K. Molyneaux, S.J. Barnett, X. Gao, Dynamic enhancement of blast-resistant ultra high performance fibre-reinforced concrete under flexural and shear loading, Inter. J. Impact Eng. 37 (4) (2010) 405–413.
[30] P.H. Bischoff, S.H. Perry, Compressive behaviour of concrete at high strain rates, Mater. Struct. 24 (6) (1991) 425–450.
[31] W. Suaris, S.P. Shah, Strain-rate effects in fibre-reinforced concrete subjected to impact and impulsive loading, Composites 13 (2) (1982) 153–159.
[32] V.S. Gopalaratnam, S.P. Shah, Properties of steel fiber reinforced concrete subjected to impact loading, J. Proc. 83 (1) (1986) 117–126.
[33] Z.L. Wang, Y.S. Liu, R.F. Shen, Stress–strain relationship of steel fiber-reinforced concrete under dynamic compression, Constr. Build. Mater. 22 (5) (2008) 811–819.
[34] V. Bindiganavile, N. Banthia, Impact response of the fiber-matrix bond in concrete, Can. J. Civ. Eng. 32 (5) (2005) 924–933.
[35] D.J. Kim, S. El-Tawil, A.E. Naaman, Rate-dependent tensile behavior of high performance fiber reinforced cementitious composites, Mater. Struct. 42 (3) (2009) 399–414.
[36] G. Plauk, B. fuer Materialpruefung, Concrete structures under impact and impulsive loading, No. INIS-mf—7709, Bundesanstalt fuer Materialpruefung, Berlin (Germany, FR), 1982.
[37] L.J. Malvar, C.A. Ross, Review of strain rate effects for concrete in tension, Mater. J. 95 (6) (1998) 735–739.
[38] S.H. Park, D.J. Kim, S.W. Kim, Investigating the impact resistance of ultra-high-performance fiber-reinforced concrete using an improved strain energy impact test machine, Constr. Build. Mater. 125 (2016) 145–159.
[39] K. Wille, A.E. Naaman, Fracture energy of UHP-FRC under direct tensile loading, Fram. -7 Inter. Confer (2010) 65–72.

[40] A.J. Zieliński, Fracture of concrete and mortar under uniaxial impact tensile loading, Delft University Press, 1982.
[41] N.T. Tran, T.K. Tran, J.K. Jeon, J.K. Park, D.J. Kim, Fracture energy of ultra-high-performance fiber-reinforced concrete at high strain rates, Cem. Concr. Res. 79 (2016) 169–184.
[42] M. Xu, K. Wille, Fracture energy of UHP-FRC under direct tensile loading applied at low strain rates, Compos. Part B 80 (2015) 116–125.
[43] K. Wille, S. El-Tawil, A.E. Naaman, Properties of strain hardening ultra high performance fiber reinforced concrete (UHP-FRC) under direct tensile loading, Cem. Concr. Compos 48 (2014) 53–66.
[44] S. Pyo, K. Wille, S. El-Tawil, A.E. Naaman, Strain rate dependent properties of ultra high performance fiber reinforced concrete (UHP-FRC) under tension, Cem. Concr. Compos 56 (2015) 15–24.
[45] R.J. Thomas, A.D. Sorensen, Review of strain rate effects for UHPC in tension, Constr. Build. Mater. 153 (2017) 846–856.